Journal of Catalysis 383 (2020) 97–102

Contents lists available at ScienceDirect

Journal of Catalysis

journal homepage: www.elsevier.com/locate/jcat

Enhancing syngas-to-aromatics performance of ZnO&H-ZSM-5 composite catalyst via Mn modulation

Yi Fu [a,b,c,1], Youming Ni [a,b,1], Wenliang Zhu [a,b], Zhongmin Liu [a,b,*]

[a] National Engineering Laboratory for Methanol to Olefins, Dalian Institute of Chemical Physics, Chinese Academy of Sciences, Dalian 116023, China
[b] Dalian National Laboratory for Clean Energy, Dalian Institute of Chemical Physics, Chinese Academy of Sciences, Dalian 116023, China
[c] University of Chinese Academy of Sciences, Beijing 100049, China

ARTICLE INFO

Article history:
Received 14 August 2019
Revised 27 December 2019
Accepted 28 December 2019
Available online 31 January 2020

Keywords:
Syngas
Aromatics
ZnO
H-ZSM-5
Manganese modulation

ABSTRACT

Application of cheap and environmentally friendly ZnO to oxide–zeolite composite catalysts for the syngas-to-aromatics (STA) reaction is still challenging. Here, we report 80.1% aromatics in products excluding CO_2, with 14.8% CO conversion over a mixed composite catalyst containing H-ZSM-5 and nanosized porous ZnO modulated by Mn. As little as 0.6–3.0 wt% of Mn can lead to a dramatic decrease in the particle size of ZnO and an obvious increase in oxygen vacancies. Mn species themselves do not act as the primary catalytic sites. The ability to convert syngas is positively correlated with oxygen vacancy concentration, whereas the ability to hydrogenate olefins is negatively correlated with it. The porous aggregated nanoparticles of ZnO modulated by Mn are resistant to sintering during syngas conversion. This provides a new strategy for STA catalyst design.

1. Introduction

Aromatics are indispensable basic chemicals, which are widely used for production of rubbers, plastic, fiber, and so on. At present, aromatics are mainly obtained by naphtha catalytic reforming and oil cracking [1,2]. Due to the growing demands for aromatics and the exhaustion of petroleum resources, production of aromatics from nonpetroleum resources, such as natural gas, coal, and biomass, is necessary and important. Syngas (CO and H_2) is usually utilized as a platform for use of nonpetroleum resources and can be converted into various valuable chemicals and fuels by traditional Fischer–Tropsch synthesis, but aromatics can hardly be synthesized [3–7]. Some composite catalysts such as ZrO_2(Zn-Cr)/H-ZSM-5 [8], Fe/MnO-GaZSM-5 [9], and Fe-Pd/H-ZSM-5 [10] have been applied to synthesize aromatics from syngas; however, their catalytic performance was unsatisfactory.

Recently, Bao et al. [11] and Wang et al. [12] reported high selectivity to C_2–C_4 olefins from syngas over $ZnCrO_x$/MSAPO-34 and $ZnZrO_x$/SAPO-34 bifunctional composite catalysts. This concept of catalyst design has been applied to the STA reaction. Wang et al. [13] reported about 80% aromatics selectivity in syngas conversion over Zn–ZrO_2/H-ZSM-5. At the same time, Ma et al. [14] reported about 51% aromatics over Na-Zn-Fe_5C_2/H-ZSM-5. Since then, a lot of oxide/zeolite composite catalysts have been developed for the STA reaction [15–19]. Among these, a small amount of Zn is generally contained in the oxides. Higher Zn content is always considered to be disadvantageous for forming aromatics as a result of the corresponding enhancement for the hydrogenation of lower olefin intermediates into paraffins [12,13,18,20,21]. Considering that ZnO itself is cheap and environmentally friendly, it is valuable to investigate the performance of bulk ZnO-derived bifunctional composite catalysts for STA reactions. Furthermore, studying the mechanism of syngas activation over ZnO is helpful in understanding and developing some industrial catalysts such as $CuZnAlO_x$ methanol synthesis catalyst [22–24]. Recent findings showed that reducing the particle size of ZnO favored the inhibition of deep hydrogenation, but particles tended to sinter more easily, resulting in rapid deactivation of composite catalysts [25]. Up to now, ZnO and H-ZSM-5 composite catalysts have not been applied successfully in STA reactions.

Here, we report 80.1% aromatics in products, excluding CO_2, with 14.8% CO conversion over a mixed composite catalyst containing H-ZSM-5 and nanosized porous ZnO modulated by Mn. A very small amount of Mn can lead to a dramatic decrease in the particle size of ZnO and an obvious increase in oxygen vacancies, which are beneficial for the suppression of deep hydrogenation. This nanosized porous structure is also resistant to sintering.

* Corresponding author at: National Engineering Laboratory for Methanol to Olefins, Dalian Institute of Chemical Physics, Chinese Academy of Sciences, Dalian 116023, China.
E-mail addresses: wlzhu@dicp.ac.cn (W. Zhu), liuzm@dicp.ac.cn (Z. Liu).
[1] Yi Fu and Youming Ni contributed equally to this work.

https://doi.org/10.1016/j.jcat.2019.12.044
0021-9517/

2. Experimental

2.1. Catalyst preparation

Mn-modulated nanosized porous ZnO catalysts were synthesized by a conventional co-precipitation method. Typically, solution I was prepared from 89.3 g of $Zn(NO_3)_2{\cdot}6H_2O$ and 6.9 g of 50 wt% manganese nitrate dissolved in 150 mL of deionized water, and solution II was made from 94.9 g of NH_4HCO_3 dissolved in 1200 mL of deionized water. They were separately dropped into a single beaker at 303 K under continuous stirring. The value of pH was kept at 7.0–7.2. The resulting precipitate was aged at this temperature for 1 h. After being filtered and washed thoroughly, the obtained mixture was dried at 333 K overnight and then calcined at 823 K for 4 h. The resulting powder oxide with about 3.0 wt% Mn was named ZnO-3. Other ZnO-*X* oxides with various weight percentages of Mn were prepared and named similarly. ZnO was prepared according to similar procedures except for not introducing Mn.

3%Mn–Al_2O_3 was prepared with procedures similar to those for ZnO–X. 3%Mn–ZnO was prepared by an impregnation method. In brief, 0.53 g of 50 wt% manganese nitrate aqueous solution was added to 2.0 g of ZnO. After 3 h with stirring, the resultant mixture was dried overnight at 333 K and finally calcined in air at 823 K for 4 h. 3%Mn–SiO_2 was prepared by a sol–gel process. Typically, solution III was prepared by mixing 13.9 g of TEOS, 1.0 g of 50 wt% manganese nitrate aqueous solution, and 20 mL ethanol. Solution IV was made by mixing 20 mL of H_2O, 25 mL of ammonia (25 wt %), and 30 mL of ethanol. Solution III was rapidly added into Solution IV under continuous stirring; the resulting precipitate was filtered and washed thoroughly. The obtained powder was dried at 333 K overnight and finally calcined at 823 K for 4 h. The Mn content in 3%Mn–Al_2O_3, 3%Mn–SiO_2, or 3%Mn–ZnO was about 3.0 wt%. H-ZSM-5 zeolite (Si/Al = 96) was the same as in our recent work [26].

Composite catalysts were prepared by physical mixing. The weight ratio of oxides and zeolites was 3:1. For the preparation of the composite catalyst ZnO-3&H-ZSM-5, ZnO-3 oxide and H-ZSM-5 zeolite were ground in an agate mortar for 4 min, pressed under 40 MPa, and granulated into the required size, in the range of 0.3–0.5 mm.

2.2. Catalytic tests

All the reactions were performed in a fixed-bed stainless steel tubular reactor (inner diameter 8 mm). All reaction products were heated to the gas phase and analyzed by an online gas chromatograph (Agilent 7890B), which was equipped with a PoraPLOT Q-HT capillary column connected to a flame ionization detector (FID) and a TDX-1 packed column connected to a thermal conductivity detector (TCD). Ar was used as an internal standard gas, CO conversion and CO_2 selectivity were calculated according to the number of carbon atoms:

$$\mathrm{Conv}_{CO} = \frac{(CO_{inlet} - CO_{outlet})}{CO_{inlet}} \times 100\%, \quad (1)$$

where CO_{inlet} is moles of CO at the inlet and CO_{outlet} is moles of CO at the outlet, and

$$\mathrm{Sel}_{CO_2} = \frac{CO_{2outlet}}{CO_{inlet} - CO_{outlet}} \times 100\%, \quad (2)$$

where $CO_{2\ outlet}$ is moles of CO_2 at the outlet. The distribution of hydrocarbons (C_nH_m), MeOH, or DME is based on the total carbon atoms of the products detected by FID.

2.3. Characterization of catalysts

X-ray diffraction (XRD) patterns were recorded on a PANalytical X'Pert PRO X-ray diffractometer with CuKα radiation. The average crystal size of the catalysts was estimated by the Scherrer equation. The elemental content of the catalysts was determined by X-ray fluorescence (XRF) on a PhilipsMagix-601 spectrometer. The surface morphology of catalysts was obtained with a field-emission scanning electron microscope (FE-SEM, SU8020). Transmission electron microscopy images (TEM) and elemental mappings were obtained on a JEM-2100F microscope. The BET specific surface areas and microspore volume were detected by a Micromeritics ASAP 2020 system. The H_2 temperature-programmed reduction profiles (H_2 TPR) were tested by Micromeritics AutoChem II 2920 equipment. X-ray photoelectron spectroscopy (XPS) analysis was done by a Thermofisher ESCALAB 250Xi spectrometer. The room-temperature photoluminescence (PL) spectra of the samples were obtained from a PTI QuantaMaster 400 photoluminescence spectrometer with a Xe lamp.

3. Results and discussion

3.1. Catalytic results

The catalytic performance of ZnO-*X* oxides was compared at 613 K, 3.0 MPa, and space velocity 2000 mL g^{-1} h^{-1}. As shown in Fig. 1a, the primary products for all these oxides are MeOH and DME, which can be slightly increased by introducing 0.6–3.0 wt% of Mn. Interestingly, after they are mixed with H-ZSM-5 zeolite, the catalytic behaviors for the resultant composite catalysts are quite different (Fig. 1b). ZnO&H-ZSM-5 shows low CO conversion (2.6%) with paraffins as predominant products, excluding CO_2. Compared with ZnO&H-ZSM-5, ZnO-*X*&H-ZSM-5 presents much better aromatization performance. The aromatics in the products, excluding CO_2, reach 74.7% with 12.6% CO conversion over ZnO-3&H-ZSM-5. The function of a little Mn in ZnO not only favors the activation of syngas but also benefits the formation of unsaturated aromatics, which suggests that the Mn species might have a great influence on the structural characteristics of ZnO. As shown in Fig. 1c, the CO conversion and aromatics over 3%Mn–Al_2O_3&H-ZSM-5 or 3%Mn–SiO_2&H-ZSM-5 are much lower than those over ZnO-3&H-ZSM-5, indicating that Mn species themselves are not the primary catalytic sites. The impregnated oxide 3%Mn–ZnO mixed with H-ZSM-5 also shows poor STA performance, suggesting that the contacting surfaces of Mn species and ZnO are also inactive. Therefore, it can be inferred that the Zn species in ZnO-3 actually play a key role in the composite catalyst. The aromatics with 9–10 carbon atoms are predominant over ZnO-3&H-ZSM-5 (Fig. S1 in the Supporting Information). An 80.1% aromatics selectivity is obtained with 14.8% CO conversion at space velocity 750 mL g^{-1} h^{-1}, which achieves almost the highest aromatics selectivity reported in the previous literature (Table S1). Increasing the space velocity can result in decreasing the aromatics but increasing the MeOH, DME, and lower olefins, which may be related to the intermediates for synthesizing aromatics (Fig. S2). Raising the reaction temperature can improve the CO conversion, but be harmful for aromatization (Fig. S3). Higher reaction pressure and a lower H_2/CO ratio are advantageous for the synthesis of aromatics from syngas (Figs. S4 and S5). The optimum weight ratio of ZnO-3 and H-ZSM-5 is 3:1 (Fig. S6). Increasing the proximity of the two components of oxides and zeolites can simultaneously enhance the CO conversion and aromatics selectivity (Fig. S7). Furthermore, it can be seen from Fig. 1d that the ZnO-3&H-ZSM-5 is durable and only has slight deactivation in a 100-h reaction test.

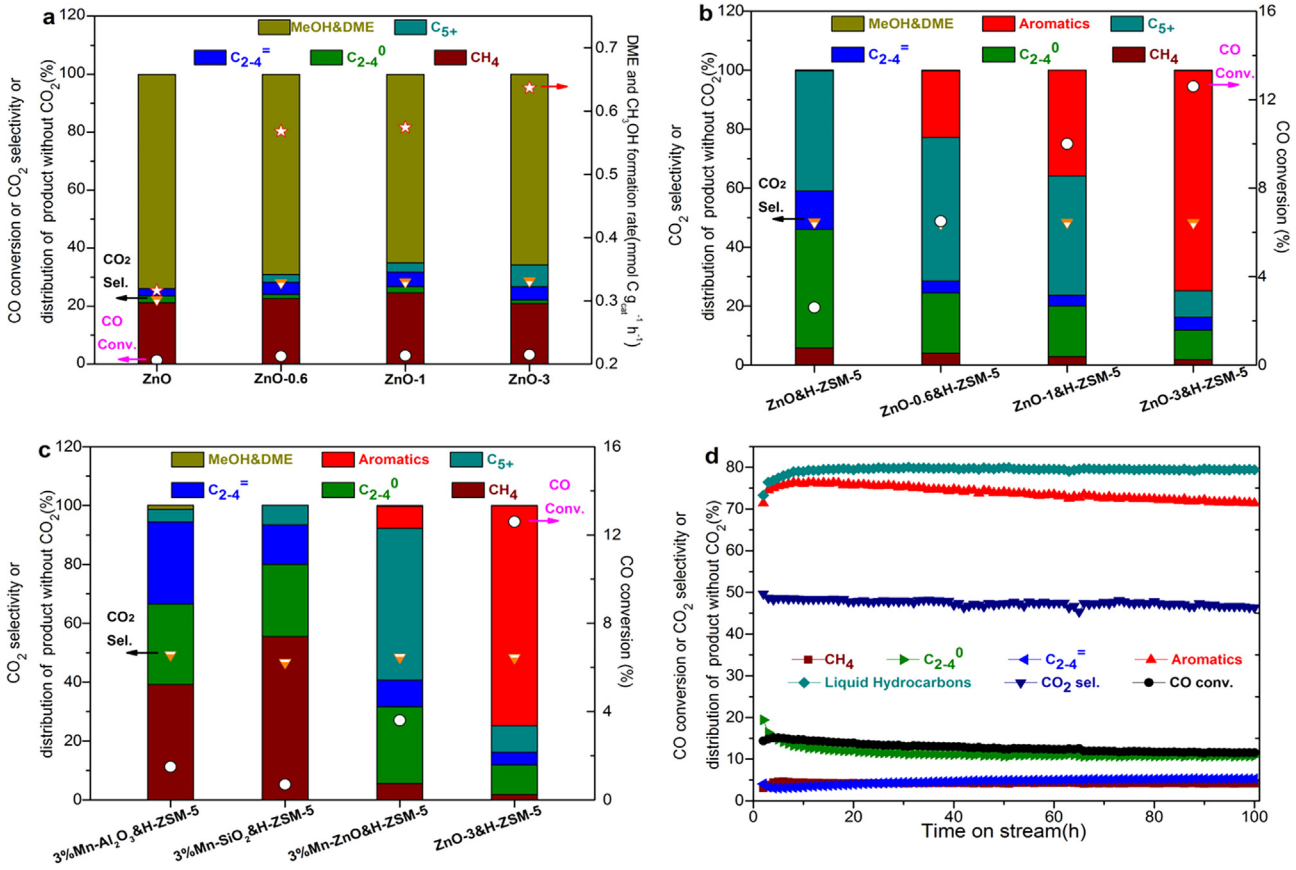

Fig. 1. Catalytic results for syngas conversion. (a) Syngas conversion over oxides at 613 K, 3.0 MPa, H_2/CO/Ar (molar ratio) = 47.5/47.5/5, space velocity = 2000 mL g^{-1} h^{-1}. (b) Syngas conversion over composite catalysts at 613 K, 3.0 MPa, H_2/CO/Ar = 47.5/47.5/5, space velocity = 1500 mL g^{-1} h^{-1}. (c) Syngas conversion over composite catalyst containing H-ZSM-5 and various oxides with 3.0 wt% Mn at 613 K, 3.0 MPa, H_2/CO/Ar = 47.5/47.5/5, space velocity = 1500 mL g^{-1} h^{-1}. (d) The stability test for ZnO-3&H-ZSM-5 at 603 K, 3.0 MPa, H_2/CO/Ar = 47.5/47.5/5, space velocity = 750 mL g^{-1} h^{-1}. Note that $C^{=}_{2-4}$ and C^{0}_{2-4} refer to C_{2-4} olefins and paraffins, respectively. The C_{5+} excludes aromatics. The *X* in ZnO-*X* denotes as the weight percentage of Mn.

3.2. Structural characterization

The XRD patterns (Figs. 2a and S8) indicate that ZnO-*X* oxides are of the typical hexagonal wurtzite phase. No additional phases of Mn were observed, indicating the high dispersion of Mn in ZnO-*X* oxides [27].

The FE-SEM images (Figs. 2b and S9) show that ZnO consists of nonporous nanoparticles with a size of 60–100 nm. Notably, the introduction of a little Mn can lead to a significant change in the morphology and an obvious decrease in crystal size. ZnO-*X* oxides present porous flowerlike structures that are formed by stacking nanoparticles. Moreover, as depicted in Table S1, the average crystal size decreased sharply from 68.9 to 20.9 nm (calculated by the Scherrer equation) after the introduction of 3.0 wt% Mn into ZnO.

The results from N_2 physical adsorption–desorption tests (Fig. 2c and Table S2) show that ZnO is nonporous (0.01 cm^3 g^{-1}) with a very low BET specific surface area (5.6 m^2 g^{-1}). Surprisingly, adding 0.6–3.0 wt% of Mn can greatly increase the pore volumes (~4–13 times) and BET specific surface areas (~2–5 times).

The TEM images in Fig. S10 give us the fact that ZnO-3 is composed of nanoparticles with an average size of about 20 nm. The lattice spacing of 0.163, 0.192, 0.248, and 0.281 nm in HRTEM images (Figs. 2d and S11) can be ascribed to the (1 1 0), (0 1 2), (0 1 1), and (0 1 0) planes of ZnO, respectively. No significant Mn clustering can be observed. The EDS mappings (Fig. S12) indicate that 3.0 wt% of Mn in ZnO-3 are highly dispersed, which is consistent with the XRD results (Fig. 2a).

Bao et al. [25] reported that ZnO with an average crystal size of about 20 nm aggregated to 31 nm after 24 h in the syngas-to-olefins reaction, leading to rapid deactivation of the composite catalyst. The smaller the size of ZnO, the more severe is the aggregation. Notably, the nanosized structures of ZnO-*X* oxides are very stable and their crystal sizes are almost unchanged after 24 h reaction, suggesting that compared with conventional dispersed nanoparticles of ZnO, these porous aggregated nanoparticles of ZnO-*X* are more resistant to sintering (Figs. S13 and S14 and Table S1).

As shown in Fig. 3a, two distinct peaks can be divided from the O1*s* XPS spectra of oxides. One peak at a lower binding energy of 529.7 ± 0.3 eV is attributed to the lattice oxygen atoms ($O_{lattice}$) [28], while another peak located at a higher binding energy of 531.3 ± 0.3 eV is generally deemed to represent the oxygen atoms adjacent to an oxygen vacancy ($O_{vacancy}$) [29,30]. It is obvious that the proportions of the $O_{vacancy}$ peak for these oxides are different, suggesting that their oxygen vacancy concentrations could be quite different. According to the calculated results from the deconvolution of the O1*s* XPS signal (Table S3) [31], the oxygen vacancy concentration can be increased with increasing Mn content, and it reaches up to 66.6% for ZnO-3. PL spectra for ZnO-*X* in Fig. 3b exhibit blue emission peaks at 415–435 nm, which can be assigned to the recombination of the photogenerated holes with the electron-occupied oxygen vacancies. That is, the higher PL peak intensity indicates a higher oxygen vacancy concentration [32–34]. It can be seen from Fig. 3b that the oxygen vacancy concentration follows

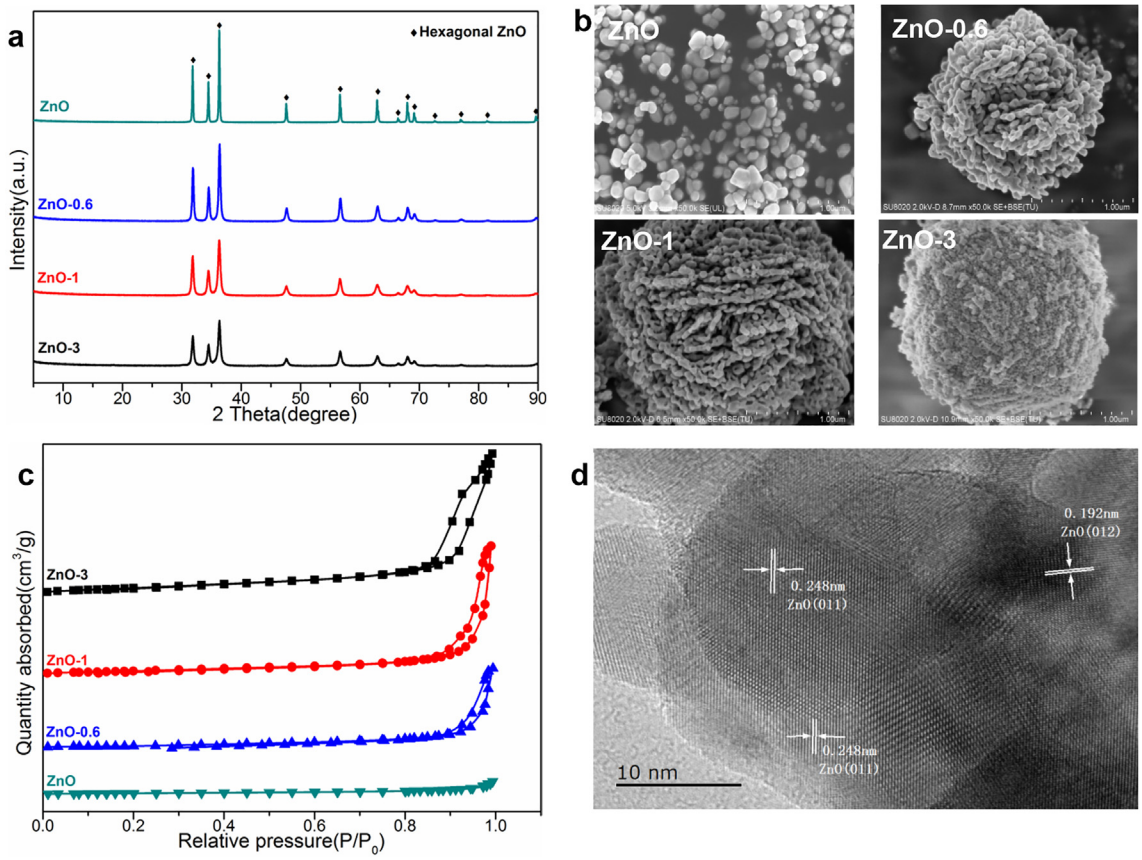

Fig. 2. Structural characterization of oxides. (a) XRD patterns. (b) FE-SEM images. (c) N_2 adsorption–desorption isotherms. (d) HRTEM image of ZnO-3.

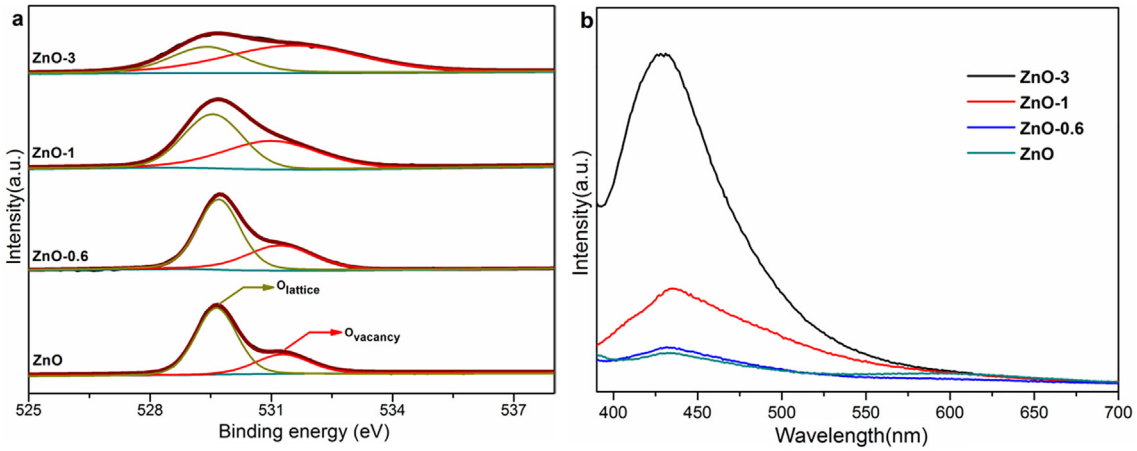

Fig. 3. The results of oxygen vacancies characterization for oxides. (a) The O1*s* XPS spectra. $O_{lattice}$ denotes the lattice oxygen atoms; $O_{vacancy}$ denotes the oxygen atoms adjacent to oxygen vacancies. (b) The room-temperature photoluminescence spectra.

the order ZnO-3 > ZnO-1 > ZnO-0.6 > ZnO, which is quite consistent with the XPS results in Fig. 3a. Moreover, the lowest reduction temperature for ZnO-3 in H_2 TPR results (Fig. S15) also shows its highest oxygen vacancy concentration, because the increase in the oxygen vacancies could promote the reducibility of oxides [35,36].

In combination with the CO conversion over ZnO-*X*&H-ZSM-5 and the oxygen vacancy concentration of ZnO-*X*, it can be found from Fig. 4 that the former increases linearly with the increase of the latter. This suggests that the oxygen vacancies of ZnO-*X* could be the principal sites for activating syngas. Actually, syngas conversion over oxides can also follow a similar rule (Fig. S16), which coincides with previous studies where high oxygen vacancy concentrations of some oxides favored the formation of MeOH and DME in syngas conversion [37,38]. It is very interesting to see that the C_3H_6 hydrogenation ability decreases monotonically with increasing oxygen vacancy concentration. That is, a high oxygen vacancy concentration is beneficial for suppressing further hydrogenation of olefins, which facilitates the formation of more olefins [25,35]. Considering that the lower olefins could act as

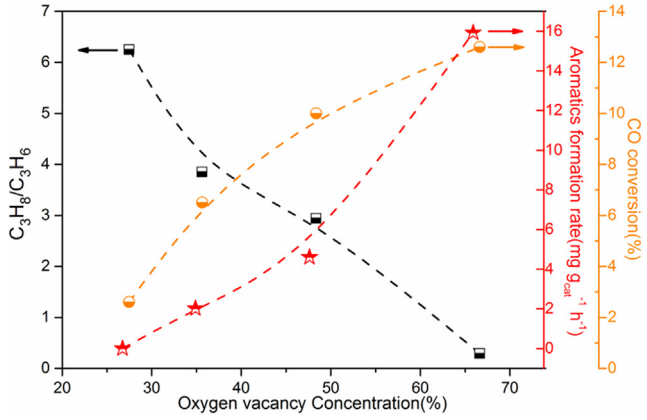

Fig. 4. The relationship between CO conversion, the aromatics formation rate for STA reaction over oxides&H-ZSM-5 or the ability of C_3H_6 hydrogenation over oxides, and the oxygen vacancy concentrations of the corresponding oxides. STA reaction conditions: 613 K, 3.0 MPa, H_2/CO/Ar = 47.5/47.5/5, space velocity = 1500 mL g^{-1} h^{-1}. C_3H_6 hydrogenation conditions: 613 K, 3.0 MPa, $H_2/C_3H_6/N_2$ (molar ratio) = 4/1/19, space velocity = 7500 mL g^{-1} h^{-1}. C_3H_8/C_3H_6 denotes the molar ratio of C_3H_8 and C_3H_6 in the effluent of C_3H_6 hydrogenation.

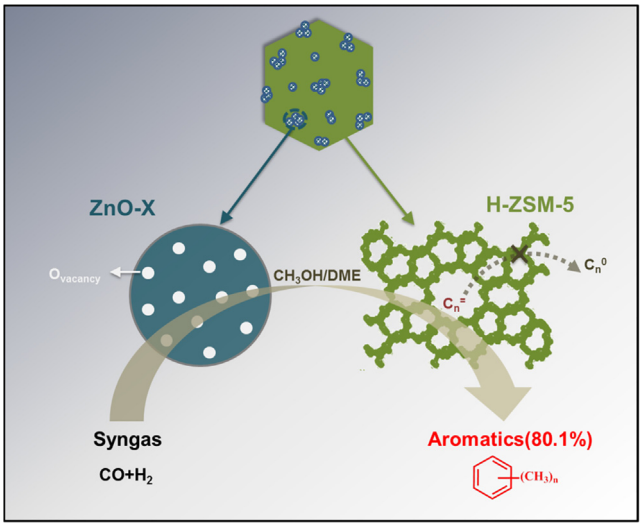

Scheme 1. Illustration of the mechanism for the STA reaction over nanoporous ZnO-*X* & H-ZSM-5.

intermediates to form aromatics, more lower olefins can be continuously converted to aromatics and it is easy to understand that the oxygen vacancy favors aromatization, as shown in Fig. 4.

According to the findings above, we propose a possible mechanism for the conversion of syngas to aromatics over ZnO-*X*&H-ZSM-5, as shown in Scheme 1. First, CO is hydrogenated to MeOH/DME over the oxygen vacancy sites of ZnO-*X*; subsequently, lower olefins can readily be synthesized when they are transmitted to H-ZSM-5; finally, most of the lower olefins can be converted continuously to aromatics because adequate oxygen vacancies for ZnO-*X* are beneficial for suppressing their further hydrogenation.

4. Conclusions

In summary, 80.1% aromatics in products (excluding CO_2) can be achieved with 14.8% CO conversion over Mn-modulated nanoporous ZnO-*X*&H-ZSM-5 composite catalysts. As little as 0.6–3.0 wt% of Mn can lead to a dramatic decrease in the particle size of ZnO and an obvious increase of oxygen vacancies. Mn species themselves do not act as the primary catalytic sites. The ability to convert syngas is positively correlated with oxygen vacancy concentration, whereas the ability to hydrogenate olefins is negatively correlated with it. The porous aggregated nanoparticles of ZnO-*X* are resistant to sintering during syngas conversion.

Declaration of Competing Interest

The authors declare that they have no known competing financial interests or personal relationships that could have appeared to influence the work reported in this paper.

Acknowledgments

We acknowledge financial support from the National Natural Science Foundation of China (Grant 21606224) and the "Transformational Technologies for Clean Energy and Demonstration" Strategic Priority Research Program of the Chinese Academy of Sciences (Grant XDA21030100).

Appendix A. Supplementary material

Supplementary data to this article can be found online at https://doi.org/10.1016/j.jcat.2019.12.044.

References

[1] A.M. Niziolek, O. Onel, Y.A. Guzman, C.A. Floudas, Biomass-based production of benzene, toluene, and xylenes via methanol: process synthesis and deterministic global optimization, Energy Fuels 30 (2016) 4970–4998.
[2] Y.M. Jia, J.W. Wang, K. Zhang, S.B. Liu, G.L. Chen, Y.F. Yang, C.M. Ding, P. Liu, Catalytic conversion of methanol to aromatics over nano-sized HZSM-5 zeolite modified by $ZnSiF_6{\cdot}6H_2O$, Catal. Sci. Technol. 7 (2017) 1776–1791.
[3] H.M.T. Galvis, K.P. de Jong, Catalysts for production of lower olefins from synthesis gas: A review, ACS Catal. 3 (2013) 2130–2149.
[4] H.M.T. Galvis, J.H. Bitter, C.B. Khare, M. Ruitenbeek, A.I. Dugulan, K.P. de Jong, Supported iron nanoparticles as catalysts for sustainable production of lower olefins, Science 335 (2012) 835–838.
[5] L.S. Zhong, F. Yu, Y.L. An, Y.H. Zhao, Y.H. Sun, Z.J. Li, T.J. Lin, Y.J. Lin, X.Z. Qi, Y.Y. Dai, L. Gu, J.S. Hu, S.F. Jin, Q. Shen, H. Wang, Cobalt carbide nanoprisms for direct production of lower olefins from syngas, Nature 538 (2016) 84–87.
[6] R.A. Friedel, R.B. Anderson, Composition of synthetic liquid fuels. I. Product distribution and analysis of C_5–C_8 paraffin isomers from cobalt catalyst, J. Am. Chem. Soc. 72 (1950) 1212–1215.
[7] M.E. Dry, High quality diesel via the Fischer-Tropsch process - a review, J. Chem. Technol. Biotechnol. 77 (2002) 43–50.
[8] C.D. Chang, W.H. Lang, A.J. Silvestri, Synthesis gas conversion to aromatic-hydrocarbons, J. Catal. 56 (1979) 268–273.
[9] N. Guan, Y. Liu, M. Zhang, Development of catalysts for the production of aromatics from syngas, Catal. Today 30 (1996) 207–213.
[10] Q.G. Yan, Y.W. Lu, C.X. Wan, J. Han, J. Rodriguez, J.J. Yin, F. Yu, Synthesis of aromatic-rich gasoline-range hydrocarbons from biomass-derived syngas over a Pd-promoted Fe/HZSM-5 catalyst, Energy Fuels 28 (2014) 2027–2034.
[11] F. Jiao, J.J. Li, X.L. Pan, J.P. Xiao, H.B. Li, H. Ma, M.M. Wei, Y. Pan, Z.Y. Zhou, M.R. Li, S. Miao, J. Li, Y.F. Zhu, D. Xiao, T. He, J.H. Yang, F. Qi, Q. Fu, X.H. Bao, Selective conversion of syngas to light olefins, Science 351 (2016) 1065–1068.
[12] K. Cheng, B. Gu, X.L. Liu, J.C. Kang, Q.H. Zhang, Y. Wang, Direct and highly selective conversion of synthesis gas into lower olefins: design of a bifunctional catalyst combining methanol synthesis and carbon-carbon coupling, Angew. Chem. Int. Ed. 55 (2016) 4725–4728.
[13] K. Cheng, W. Zhou, J.C. Kang, S. He, S.L. Shi, Q.H. Zhang, Y. Pan, W. Wen, Y. Wang, Bifunctional catalysts for one-step conversion of syngas into aromatics with excellent selectivity and stability, Chem 3 (2017) 334–347.
[14] B. Zhao, P. Zhai, P.F. Wang, J.Q. Li, T. Li, M. Peng, M. Zhao, G. Hu, Y. Yang, Y.W. Li, Q.W. Zhang, W.B. Fan, D. Ma, Direct transformation of syngas to aromatics over Na-Zn-Fe_5C_2 and hierarchical HZSM-5 tandem catalysts, Chem 3 (2017) 323–333.
[15] J.H. Yang, X.L. Pan, F. Jiao, J. Li, X.H. Bao, Direct conversion of syngas to aromatics, Chem. Commun. 53 (2017) 11146–11149.
[16] P.P. Zhang, L. Tan, G.H. Yang, N. Tsubaki, One-pass selective conversion of syngas to para-xylene, Chem. Sci. 8 (2017) 7941–7946.
[17] Z. Huang, S. Wang, F. Qin, L. Huang, Y.H. Yue, W.M. Hua, M.H. Qiao, H.Y. He, W. Shen, H.L. Xu, Ceria-zirconia/zeolite bifunctional catalyst for highly selective conversion of syngas into aromatics, ChemCatChem 10 (2018) 4519–4524.
[18] M.T. Arslan, B.A. Qureshi, S.Z.A. Gilani, D.L. Cai, Y.H. Ma, M. Usman, X. Chen, Y. Wang, F. Wei, Single-step conversion of H_2-deficient syngas into high yield of tetramethylbenzene, ACS Catal. 9 (2019) 2203–2212.

[19] Y. Xu, J. Liu, J. Wang, G. Ma, J. Lin, Y. Yang, Y. Li, C. Zhang, M. Ding, Selective conversion of syngas to aromatics over Fe_3O_4@MnO_2 and hollow HZSM-5 bifunctional catalysts, ACS Catal. 9 (2019) 5147–5156.
[20] X.L. Liu, W. Zhou, Y.D. Yang, K. Cheng, J.C. Kang, L. Zhang, G.Q. Zhang, X.J. Min, Q.H. Zhang, Y. Wang, Design of efficient bifunctional catalysts for direct conversion of syngas into lower olefins via methanol/dimethyl ether intermediates, Chem. Sci. 9 (2018) 4708–4718.
[21] W. Zhou, K. Cheng, J. Kang, C. Zhou, V. Subramanian, Q. Zhang, Y. Wang, New horizon in C1 chemistry: breaking the selectivity limitation in transformation of syngas and hydrogenation of CO_2 into hydrocarbon chemicals and fuels, Chem. Soc. Rev. 48 (2019) 3193–3228.
[22] M. Behrens, F. Studt, I. Kasatkin, S. Kuhl, M. Havecker, F. Abild-Pedersen, S. Zander, F. Girgsdies, P. Kurr, B.L. Kniep, M. Tovar, R.W. Fischer, J.K. Norskov, R. Schlogl, The active site of methanol synthesis over Cu/ZnO/Al_2O_3 industrial catalysts, Science 336 (2012) 893–897.
[23] S. Kuld, M. Thorhauge, H. Falsig, C.F. Elkjaer, S. Helveg, I. Chorkendorff, J. Sehested, Quantifying the promotion of Cu catalysts by ZnO for methanol synthesis, Science 352 (2016) 969–974.
[24] S. Kattel, P.J. Ramirez, J.G. Chen, J.A. Rodriguez, P. Liu, Active sites for CO_2 hydrogenation to methanol on Cu/ZnO catalysts, Science 355 (2017) 1296–1299.
[25] N. Li, F. Jiao, X.L. Pan, Y. Ding, J.Y. Feng, X.H. Bao, Size effects of ZnO nanoparticles in bifunctional catalysts for selective syngas conversion, ACS Catal. 9 (2019) 960–966.
[26] Y.M. Ni, Z.Y. Chen, Y. Fu, Y. Liu, W.L. Zhu, Z.M. Liu, Selective conversion of CO_2 and H_2 into aromatics, Nat. Commun. 9 (2018) 3457.
[27] J.Z. Li, M.J. Chen, D.A. Cullen, S. Hwang, M.Y. Wang, B.Y. Li, K.X. Liu, S. Karakalos, M. Lucero, H.G. Zhang, C. Lei, H. Xu, G.E. Sterbinsky, Z.X. Feng, D. Su, K.L. More, G.F. Wang, Z.B. Wang, G. Wu, Atomically dispersed manganese catalysts for oxygen reduction in proton-exchange membrane fuel cells, Nat. Catal. 1 (2018) 935–945.
[28] C. Yang, J. Wang, H.L. Fan, S.G. Ju, J. Mi, C. Huo, Contributions of tailored oxygen vacancies in ZnO/Al_2O_3 composites to the enhanced ability for H_2S removal at room temperature, Fuel 215 (2018) 695–703.
[29] Y.F. Zhu, X.L. Pan, F. Jiao, J. Li, J.H. Yang, M.Z. Ding, Y. Han, Z. Liu, X.H. Bao, Role of Manganese Oxide in Syngas Conversion to Light Olefins, ACS Catal. 7 (2017) 2800–2804.
[30] Z.L. Wang, X. Mao, P. Chen, M. Xiao, S.A. Monny, S.C. Wang, M. Konarova, A.J. Du, L.Z. Wang, Understanding the roles of oxygen vacancies in hematite-based photoelectrochemical processes, Angew. Chem. Int. Ed. 58 (2019) 1030–1034.
[31] O. Martin, A.J. Martin, C. Mondelli, S. Mitchell, T.F. Segawa, R. Hauert, C. Drouilly, D. Curulla-Ferre, J. Perez-Ramirez, Indium oxide as a superior catalyst for methanol synthesis by CO_2 hydrogenation, Angew. Chem. Int. Ed. 55 (2016) 6261–6265.
[32] Z.Y. Xue, D.H. Zhang, Q.P. Wang, J.H. Wang, The blue photoluminescence emitted from ZnO films deposited on glass substrate by rf magnetron sputtering, Appl. Surf. Sci. 195 (2002) 126–129.
[33] F.C. Lei, Y.F. Sun, K.T. Liu, S. Gao, L. Liang, B.C. Pan, Y. Xie, Oxygen vacancies confined in ultrathin indium oxide porous sheets for promoted visible-light water splitting, J. Am. Chem. Soc. 136 (2014) 6826–6829.
[34] S. Kumar, A.K. Ojha, Room temperature ferromagnetism in undoped and Mn doped t-ZrO_2 nanostructures originated due to oxygen vacancy and effect of Mn doping on its optical properties, Mater. Chem. Phys. 169 (2016) 13–20.
[35] X.L. Liu, M.H. Wang, C. Zhou, W. Zhou, K. Cheng, J.C. Kang, Q.H. Zhang, W.P. Deng, Y. Wang, Selective transformation of carbon dioxide into lower olefins with a bifunctional catalyst composed of $ZnGa_2O_4$ and SAPO-34, Chem. Commun. 54 (2018) 140–143.
[36] X.W. Liu, K.B. Zhou, L. Wang, B.Y. Wang, Y.D. Li, Oxygen vacancy clusters promoting reducibility and activity of ceria nanorods, J. Am. Chem. Soc. 131 (2009) 3140–3141.
[37] S. Polarz, J. Strunk, V. Ischenko, M.W.E. van den Berg, O. Hinrichsen, M. Muhler, M. Driess, On the role of oxygen defects in the catalytic performance of zinc oxide, Angew. Chem. Int. Ed. 45 (2006) 2965–2969.
[38] J. Strunk, K. Kaehler, X.Y. Xia, M. Comotti, F. Schuth, T. Reinecke, M. Muhler, Au/ZnO as catalyst for methanol synthesis: The role of oxygen vacancies, Appl. Catal. A: Gen. 359 (2009) 121–128.